Applied Physics Reviews

RESEARCH ARTICLE | JANUARY 29 2024

In situ cryptography in a neuromorphic vision sensor based on light-driven memristors

Lingxiang Hu ; Jiale Shao ; Jingrui Wang ; Peihong Cheng; Li Zhang ; Yang Chai ; Zhizhen Ye; Fei Zhuge

Appl. Phys. Rev. 11, 011411 (2024)
https://doi.org/10.1063/5.0185502

In situ cryptography in a neuromorphic vision sensor based on light-driven memristors

Cite as: Appl. Phys. Rev. **11**, 011411 (2024); doi: 10.1063/5.0185502
Submitted: 31 October 2023 · Accepted: 2 January 2024 ·
Published Online: 29 January 2024

View Online Export Citation CrossMark

Lingxiang Hu,[1,2] Jiale Shao,[1] Jingrui Wang,[1,3] Peihong Cheng,[1,3] Li Zhang,[4] Yang Chai,[5] Zhizhen Ye,[6,7] and Fei Zhuge[1,2,6,8,a)]

AFFILIATIONS

[1]Ningbo Institute of Materials Technology and Engineering, Chinese Academy of Sciences, Ningbo 315201, China
[2]Center of Materials Science and Optoelectronics Engineering, University of Chinese Academy of Sciences, Beijing 100029, China
[3]School of Electronic and Information Engineering, Ningbo University of Technology, Ningbo 315211, China
[4]Healthcare Engineering Centre, School of Engineering, Temasek Polytechnic, Tampines Ave, Singapore 529757, Singapore
[5]Department of Applied Physics, The Hong Kong Polytechnic University, Hong Kong 999077, China
[6]Institute of Wenzhou, Zhejiang University, Wenzhou 325006, China
[7]State Key Laboratory of Silicon Materials, School of Materials Science and Engineering, Zhejiang University, Hangzhou 310027, China
[8]Center for Excellence in Brain Science and Intelligence Technology, Chinese Academy of Sciences, Shanghai 200072, China

[a)]Author to whom correspondence should be addressed: zhugefei@nimte.ac.cn

ABSTRACT

Vision sensors are becoming increasingly ubiquitous, and they continuously collect, store, communicate, and process vast amount of sensitive data that are vulnerable to being stolen and misused. Existing cryptosystems based on complex cipher algorithms generally require extensive computational resources, making them difficult to use in vision sensors that have limited processing capabilities. Here, we propose and experimentally demonstrate a novel *in situ* image cryptography scheme based on a neuromorphic vision sensor comprising all-optically controlled (AOC) memristors. Due to the unique light wavelength and irradiation history-dependent bidirectional persistent photoconductivity of AOC memristors, a visual image can be stored, encrypted, decrypted, denoised, and destroyed within a vision sensor. A decrypted image can be encoded *in situ* and then accurately recognized through a memristive neural network. Encrypted and destroyed images are capable of withstanding hacking attacks even with trained neural networks. Our cryptography scheme enables complete cryptographic operations entirely on a sensor and, therefore, effectively safeguards visual information. This work provides a simple yet efficient solution to the security challenges faced by vision sensors.

INTRODUCTION

In recent years, vision sensors composed of image detectors based on complementary metal–oxide–semiconductor (CMOS) or charge-coupled device (CCD) technology and digital processors and memories have promoted the rapid development of emerging intelligent systems such as the Internet of Things, robots, and autonomous driving vehicles. The large amount of sensitive personal information continuously collected by vision sensors is susceptible to unauthorized access and misuse, thus facing elevated security risks and vulnerabilities.[1] While modern cryptosystems based on intricate cipher algorithms can offer powerful security solutions,[2–4] they typically require substantial computational resources. However, vision sensors generally have simple configurations and lack the necessary computational power for the operation of cipher algorithms, rendering the utilization of modern software cryptosystems impractical.[4,5] Therefore, it is urgent to develop hardware-based security technologies that can provide robust protection that only require limited computational resources.[6–8] Such technologies should also allow seamless integration with vision sensors to ensure the security and privacy of the visual information they collect.

The emergence of bioinspired vision technologies presents a promising opportunity to address the pressing issue of information security risks.[9–15] While the optoelectronic detectors in conventional vision sensors only convert captured light signals into electronic signals, the human retina can not only detect visual images but also perform preprocessing (e.g., feature extraction) to reduce the amount of redundant information transmitted to the visual cortex of the brain, enabling efficient processing of visual information and significantly reducing the computational resources required by the brain.[16,17] Inspired by the human retina, the concept of in-sensor computing was proposed to as a way to perform part of the information processing task directly within the sensor.[18,19] The capability of in-sensor computing makes possible the realization of *in situ* cryptography within vision sensors.

There have been efforts to demonstrate in-sensor neuromorphic computing using emerging optoelectronic devices such as memristors[14,20–29] and transistors.[30–40] These devices leverage nonlinear optoelectronic responses or gate-tunable positive/negative photoconductance to implement image preprocessing, including feature extraction, denoising, and adaptive imaging.[14,24–26,30–41] Recently, an integration of optoelectronic detectors and neuromorphic processors has been demonstrated to realize high-level computing functionalities such as image encoding and recognition, in which a detector captures visual information while a processor is responsible for information processing and storage.[42–45] Nevertheless, these previously reported neuromorphic vision sensors can hardly implement information security functions due to their insufficient optoelectronic properties.

In this study, we propose and develop a neuromorphic vision sensor with *in situ* cryptographic computing capability. The sensor comprises a neuromorphic optoelectronic detector consisting of an array of all-optically controlled (AOC) memristors and a neuromorphic computing network (NCN) constructed using the feature parameters of the same memristive device. Under long-wavelength light irradiation, an AOC memristor exhibits negative persistent photoconductivity (NPPC), while under short-wavelength light, it demonstrates positive persistent photoconductivity (PPPC). More importantly, the NPPC of an AOC memristor is strongly influenced by the wavelength of the light used to trigger the PPPC. Due to this unique optoelectronic response, the AOC memristor-based optoelectronic detector enables storage, encryption, decryption, denoising, and destruction of a visual image, through irradiation with a range of characteristic wavelengths. Furthermore, the image encoding process, i.e., feature extraction, can also be completed within the detector itself. Dimensionality-reduced feature vectors can be input into the memristive NCN for image recognition. The decrypted image exhibits a recognition accuracy of over 80%. Notably, the encrypted and destroyed images prove difficult to decipher, even if a hacker gains access to the trained neural networks. We believe the proposed neuromorphic vision sensor provides a convenient and effective approach to securing vision information, with potential for extensive applications in situations where visual information is collected. It is also worth mentioning that the proposed *in situ* cryptography technique is mainly aimed at lightweight edge devices with limited computing power, which is complementary to modern visual cryptography techniques relying on computational resources.

RESULTS AND DISCUSSION

Architecture schema for *in situ* image cryptography

In a conventional vision sensor [Fig. 1(a)], an optoelectronic detector captures visual images, generating raw analog electronic signals. These signals are then converted to digital signals via an analog–digital converter before being transmitted to a post-processor with a von Neumann architecture to perform further preprocessing or recognition tasks. To address the information security issues in conventional vision sensors, we developed an in-sensor cryptography architecture that integrates image sensing, cryptographic computing, and processing functions, as shown in Fig. 1(b). The proposed vision sensor consists of two modules: a neuromorphic optoelectronic detector and an in-memory computing unit; both are constructed using AOC memristor arrays. Figure 1(c) shows the block diagrams of the image processing sequence in our vision sensor, taking the letter "A" as an example. First, the image of A is directly captured by the optoelectronic detector and stored as memristor photoconductance values. Next, the image is encrypted using light irradiation, which causes the image to lose its original characteristics. Then, the encrypted image is restored via decryption light irradiation. Finally, the decrypted image is encoded *in situ* and recognized with the in-memory computing unit. In addition, image preprocessing and destruction can also be performed within the detector. The capability of integrating multiple functions into our vision sensor is attributed to the AOC memristor's unique PPPC and NPPC effects.

AOC memristor PPPC and NPPC

Our AOC memristor is based on an oxygen-deficient InGaZnO (O_D-IGZO)/oxygen-rich InGaZnO (O_R-IGZO) homojunction, as schematically illustrated in Fig. 2(a). It shows bipolar memristive switching behavior when measured in the dark (Fig. S1). Upon short-wavelength light irradiation, it undergoes a transition from a low-memconductance state (LMS) to a high-memconductance state (HMS), which is referred to as the PPPC effect or the SET operation [Fig. 2(b)]. The device can be switched back from the HMS to the LMS via long-wavelength irradiation, which is called the NPPC effect or the RESET operation [Fig. 2(c)]. The light-induced memconductance states are nonvolatile [Fig. 2(d)]. We found that the strength of NPPC, quantitatively represented by the RESET index, is closely related to the SET light wavelength used to realize the PPPC (λ_{PPPC}), as illustrated in Figs. 2(e) and S2. Specifically, at a fixed initial memconductance, the RESET index decreases with increasing λ_{PPPC}. We also found that regardless of the previous device state (e.g., the first SET operations by 350 and 450 nm irradiation), 350 nm irradiation with a fixed power density sets the device to an almost fixed HMS (the second SET operations), as shown in Fig. S3. Moreover, the following RESET indexes are almost the same irrespective of the light wavelength for the first SET operation [Figs. 2(f) and S3]. This unique λ_{PPPC}-dependent NPPC behavior of our AOC memristor is the key to achieving in-sensor cryptography.

In our previous study,[21] we have proposed that the observed PPPC and NPPC could be attributed to the ionization and neutralization of oxygen vacancies (V_Os) in the O_D-IGZO/O_R-IGZO interfacial barrier region, respectively [Fig. 2(g)]. Specifically, short-wavelength light-induced transformation from the neutral V_Os located in the interfacial barrier region into V_O^{2+}s causes a decrease in the barrier width, thus giving rise to an increased memconductance. The nonvolatility of the light-induced memconductance states may be due to (i) the free electrons generated in the interfacial barrier region are pulled away by the built-in electric field and cannot recombine with V_O^{2+}s, and (ii) a potential barrier resulting from the outward relaxation of bonds around the oxygen vacancies needs to be overcome to neutralize

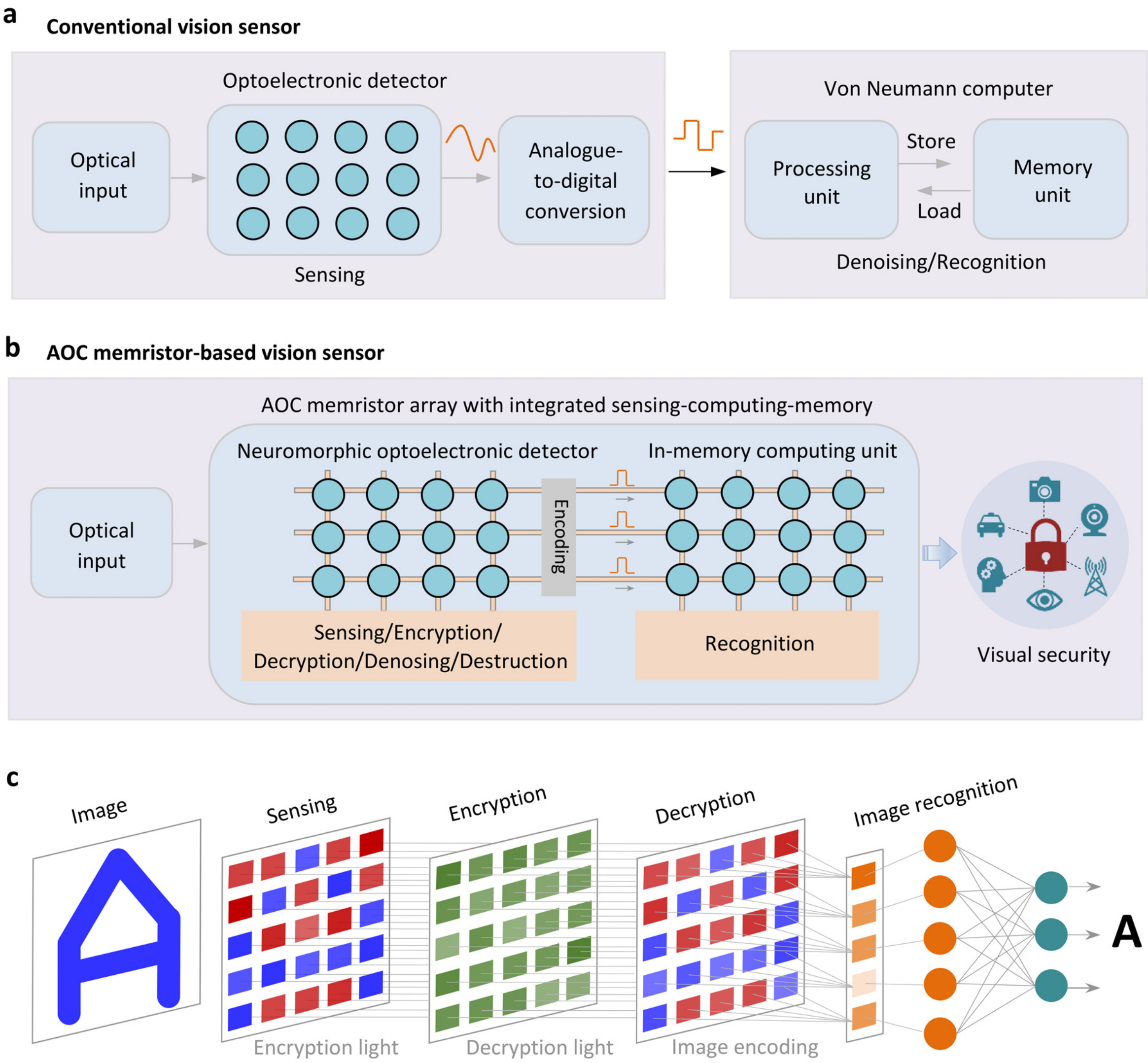

FIG. 1. *In situ* image cryptography architecture. Architecture schematics of a conventional vision sensor (a) and our AOC memristor-based vision sensor (b). (c) Block diagrams of the image processing sequence in our vision sensor taking the letter A as an example.

V_O^{2+}s. During the subsequent long-wavelength irradiation, electrons in the potential well formed by band bending of O_R-IGZO tunnel through or jump over the O_D-IGZO/O_R-IGZO interfacial barrier. These electrons are captured by V_O^{2+}s, which then transform into *V*os, leading to an increase in the barrier width and thus decreasing the memconductance. We can see from Figs. 2(b) and 2(c) that compared to the PPPC, the NPPC behavior is relatively poor. It could be explained as follows: V_O^{2+} neutralization is limited by the number of electrons injected from the potential well to the conduction band of O_D-IGZO; the O_D-IGZO/O_R-IGZO interfacial barrier severely limits the number of injected electrons, thus weakening the neutralization reaction of V_O^{2+}s. It is also worth noting that an abrupt increase in memconductance is observed when applying the long-wavelength light [Fig. 2(c)], which is likely due to the following reasons: (i) a photovoltaic voltage is generated upon light irradiation[28] (Fig. S4), and (ii) some V_Os regenerated from the spontaneous neutralization of V_O^{2+}s are ionized.[21] In fact, the ionization of V_Os and the neutralization of V_O^{2+}s occur simultaneously under both short- and long-wavelength illumination.[21] The light-induced memconductance depends on the dynamic equilibrium between these two opposite reactions. For a memristive device in the LMS, the V_O ionization is dominant, leading to a memconductance increase upon illumination. As for the device in a HMS after short-wavelength light exposure, the neutralization of V_O^{2+}s dominates upon long-wavelength irradiation, thus enabling a memconductance decrease. Herein, the V_O defects in IGZO fall into two categories: those with at least one neighboring Ga atom [$Vo_{(Ga)}$] and those without neighboring Ga atoms [$Vo_{(M)}$, M = In or Zn]. The V_O defect levels are significantly affected by the type of the neighboring metal atoms. $Vo_{(Ga)}$s have a relatively deeper defect level than $Vo_{(M)}$s[46,47] [Fig. 2(g)].

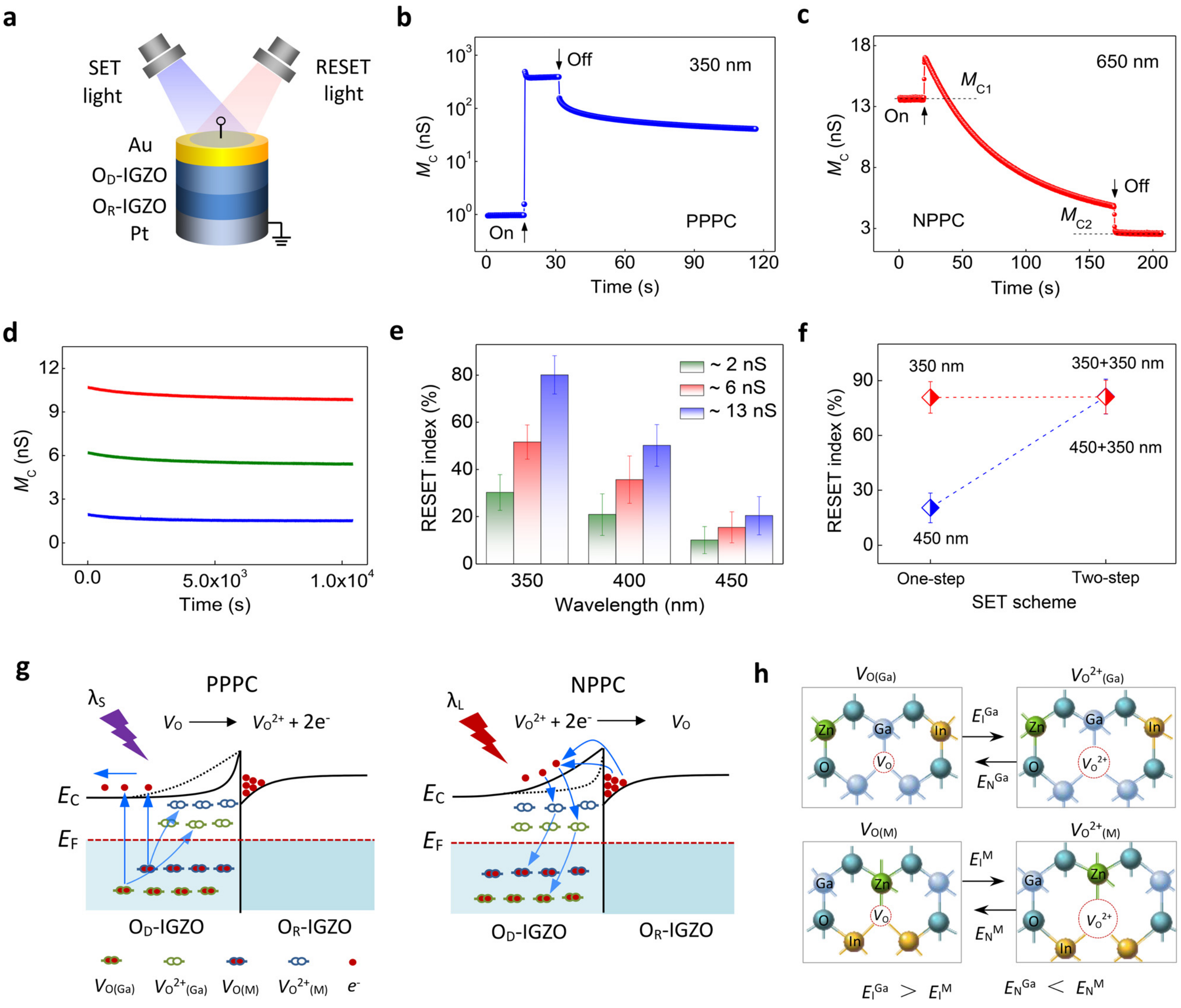

FIG. 2. PPPC and NPPC of the AOC memristor. (a) Schematic diagram of the device structure and operating mode. The SET and RESET light irradiation results in PPPC and NPPC effects, respectively. (b) PPPC behavior upon irradiation with UV light [$\lambda = 350$ nm, duration (D) = 15 s, and power density (P) = 20 μW cm^{-2}]. (c) NPPC behavior upon irradiation with red light ($\lambda = 650$ nm, D = 150 s, and P = 30 μW cm^{-2}). (d) Retention characteristics of the three memconductance states after optical RESET operations. First, the device was set to an HMS of approximately 13 nS, and then, three RESET operations were conducted with different irradiation durations of 650 nm light. After each RESET operation and subsequent retention measurement, the device was set to 13 nS again. (e) Dependence of the RESET index on the wavelength of the initial SET light. Prior to the optical RESET, the device was set to three HMSs ($M_C = 2$, 6, and 13 nS) using SET light irradiation with different durations or power densities. The RESET index values were calculated by the formula [$(M_{C1} - M_{C2})/M_{C1}$] × 100%, where M_{C1} and M_{C2} are the device memconductance before and after irradiation, respectively. (f) Comparison between the RESET indexes of the devices after one-step and two-step SET. Part of data are from Fig. S3. The duration and power density of 450 nm light are 25 s and 30 μW cm^{-2}, respectively. In (b)–(f), the memconductance values were measured at 0.1 V. (g) Schematic illustrations of the PPPC (left panel) and NPPC (right panel) mechanisms. E_C and E_F denote the conduction band minimum and Fermi energy, respectively. The black dotted lines indicate the positions of E_C before short- and long-wavelength (λ_S and λ_L) irradiation. (h) Schematic diagrams of the outward and inward relaxation of neighboring metal atoms during the ionization and neutralization of oxygen vacancies in IGZO. $Vo_{(Ga)}$ and $Vo^{2+}{}_{(Ga)}$ denote the neutral and ionized oxygen vacancies with at least one neighboring Ga atom, respectively; $Vo_{(M)}$ and $Vo^{2+}{}_{(M)}$ (M = In or Zn) denote the neutral and ionized oxygen vacancies without neighboring Ga atoms, respectively. E_I^{Ga} and E_I^{M} represent the ionization energy of $Vo_{(Ga)}$ and $Vo_{(M)}$, respectively; E_N^{Ga} and E_N^{M} represent the neutralization energy of $Vo^{2+}{}_{(Ga)}$ and $Vo^{2+}{}_{(M)}$, respectively.

In this study, we further confirm the key role of the O$_D$-IGZO/O$_R$-IGZO interface in PPPC and NPPC effects by constructing an O$_D$-IGZO/O$_R$-IGZO/O$_D$-IGZO trilayer structure. This trilayer memristive device exhibits clear PPPC and NPPC phenomena (Fig. S5). Given that Ohmic contacts are formed at the metal/O$_D$-IGZO interfaces,[21] the conduction behavior of the trilayer device should be dominated by two back-to-back symmetric O$_D$-IGZO/O$_R$-IGZO homojunctions. Hence, we conclude that PPPC and NPPC originate from photoinduced conductance change of the O_D-IGZO/O_R-IGZO interface. This conclusion is consistent with the observation that neither PPPC nor NPPC is realized in single-layered O_D-IGZO and O_R-IGZO devices.

The λ_{PPPC}-dependent NPPC in Fig. 2(e) can be explained by the local bonding environment-dependent ionization energy of neutral V_Os (E_I) and energy barrier against neutralizing $V_O{}^{2+}$ (E_N), as schematically illustrated in Fig. 2(h). We previously mentioned that the defect level of $Vo_{(Ga)}$s is deeper than $Vo_{(M)}$s (M = In or Zn), thus resulting in a higher E_I of $Vo_{(Ga)}$s ($E_I{}^{Ga}$) compared to that of $Vo_{(M)}$s ($E_I{}^{M}$).[46,47] The V_O ionization induces an outward relaxation of the neighboring metal atoms, and therefore, the following $V_O{}^{2+}$ neutralization needs to overcome an energy barrier E_N.[48,49] Theoretical calculations have shown that the E_N for $Vo^{2+}{}_{(Ga)}$ neutralization ($E_N{}^{Ga}$) is lower than that for $Vo^{2+}{}_{(M)}$ neutralization ($E_N{}^{M}$).[46,47] Then, we can deduce that the SET light irradiation at a shorter wavelength (e.g., 350 nm) converts more $Vo_{(Ga)}$s into $Vo^{2+}{}_{(Ga)}$s since $E_I{}^{Ga} > E_I{}^{M}$. Considering that the pristine device is set to the same HMS (e.g., ∼13 nS) by the SET light irradiation with different wavelengths, the incremental number of Vo^{2+}s at a fixed HMS should be the same regardless of SET light wavelength. Given that $Vo^{2+}\text{s} = Vo^{2+}{}_{(Ga)}\text{s} + Vo^{2+}{}_{(M)}\text{s}$, more $Vo^{2+}{}_{(Ga)}$s and less $Vo^{2+}{}_{(M)}$s are formed in the O_D-IGZO/O_R-IGZO interfacial barrier region upon SET light irradiation with a shorter wavelength. When the device is subsequently exposed to the RESET light, more $V_O{}^{2+}$s are converted into neutral V_Os since $E_N{}^{Ga} < E_N{}^{M}$, resulting in a wider interfacial barrier region and thus increasing the RESET index [Figs. 2(g) and 2(h)]. The SET scheme-independent NPPC in Fig. 2(f) (two-step SET), and Fig. S3 indicates that the memristive devices in different memconductance states can be set to similar HMSs concerning both memconductance values and defect states including $Vo_{(Ga)}$s, $Vo^{2+}{}_{(Ga)}$s, $Vo_{(M)}$s, and $Vo^{2+}{}_{(M)}$s.

In situ image encryption and decryption

Figure 3(a) provides a schematic representation of the physical implementation of in-sensor encryption and decryption using a 5 × 5 AOC memristor array (Fig. S6), where each memristor cell corresponds to a single image pixel. The experimental results, which demonstrate the effectiveness of the encryption and decryption processes, are presented in Figs. 3(b) and 3(c). A memconductance readout circuit is used to measure the memconductance of each pixel and is described in detail in Materials and Methods and Fig. S6. Initially, all the pixels are in similar LMSs. The letter A is mapped directly onto the array in the form of memconductance with an imaging light (blue; $\lambda = 450$ nm, D = 25 s, and P = 30 μW cm^{-2}), which converts the pixels with blue light exposure from their initial LMSs to HMSs while leaving the remaining pixels in their LMSs. The AOC memristor array can store the image *in situ* after the irradiation is stopped (Fig. S7), which is not possible with conventional optoelectronic detectors. Next, ultraviolet (UV) light ($\lambda = 350$ nm, D = 15 s, and P = 20 μW cm^{-2}) is used to encrypt the image by selective irradiation of the pixels without blue light exposure. The encryption light irradiation increases the memconductance of these pixels to values similar to those of blue light-irradiated pixels, thereby hiding the image. After encryption, the memconductance of each pixel exhibits a consistent tendency, demonstrating good encrypted image retention performance, as shown in Fig. 3(b). Finally, the encrypted image can be decrypted by irradiating all pixels with red light, taking advantage of the λ_{PPPC}-dependent NPPC of the AOC memristor. Specifically, the UV light-irradiated pixels demonstrate lower memconductance upon subsequent red light irradiation due to larger RESET indexes compared to the blue light-irradiated pixels, allowing the image to be recovered from the encryption state. Figure 3(c) illustrates the dynamic decryption process, where the decrypted image gradually becomes clearer with increasing irradiation time.

To provide a more comprehensive explanation of the decryption process and its efficiency, we calculated the RESET rates of all 25 pixels, as shown in Fig. 3(d). Herein, the RESET rate indicates the instantaneous rate of memconductance decrease. Clearly, the UV light-irradiated pixels exhibit higher RESET rates than the blue light-irradiated pixels, especially in the initial stage of red light irradiation. Moreover, both types of pixels' RESET rates decrease as the red light irradiation time increases, with the UV light-irradiated pixels decreasing more rapidly, resulting in an overlap at approximately 150 s. This suggests that the memconductance differences ($\triangle M_C$) between the two types of pixels increase with the red light irradiation time and peak at 150 s. To evaluate the image decryption efficiency, we then calculated the average $\triangle M_C$ at different times as shown in Fig. 3(e). As expected, the average $\triangle M_C$ increases gradually with decryption time and approaches saturation at 150 s. Additionally, we performed the encryption and decryption of the letters from "B" to "Z" with the same AOC memristor array (Fig. S8). Figure 3(f) shows the average $\triangle M_C$ of all 26 letters in the alphabet, with a fixed decryption time of 150 s. The $\triangle M_C$ value fluctuates in a narrow range, indicating good robustness in the encryption/decryption scheme and excellent AOC memristor operational stability.

Image encoding and recognition

To recognize the decrypted images, an AOC memristor-based NCN was utilized, as schematically illustrated in Fig. 4(a). To simplify the training process and reduce the computational burden, a straightforward image encoding approach was adopted. Specifically, a five-dimensional image feature vector was obtained by summing the pixel currents row-wise. Herein, the current of each pixel was read out using a fixed voltage. The feature vectors of the detected, encrypted, and decrypted images of the letter A are presented in Figs. 4(b)–4(d), respectively. Each feature vector consists of five normalized current values. Additionally, Fig. 4(e) illustrates the encoding results of all 26 letters of the alphabet for the detected, encrypted, and decrypted images. Notably, the detected and decrypted images exhibit distinguishable feature vectors, whereas the feature vectors of the encrypted images are difficult to differentiate from each other, confirming the effectiveness of the proposed encoding method for the 26 letters.

To facilitate subsequent image recognition, a three-layer NCN was constructed using our AOC memristors [Figs. 4(a) and S9(a)]. The synaptic weight (represented as the memconductance) tuning properties were determined by subjecting the device to 10 memconductance increase/decrease cycles, as shown in Fig. 4(f). The AOC memristor's reversible tuning of the memconductance was achieved via blue and red light irradiation, utilizing the PPPC and NPPC effects [Fig. S9(b)]. To verify the usability of the AOC memristor-based NCN, two standard datasets were used to train the NCN, i.e., 8 × 8 (Ref. 50) and 28 × 28 (Ref. 51) pixel images of handwritten digits. As shown in Figs. S9(c) and S9(d), the recognition accuracies for both small and

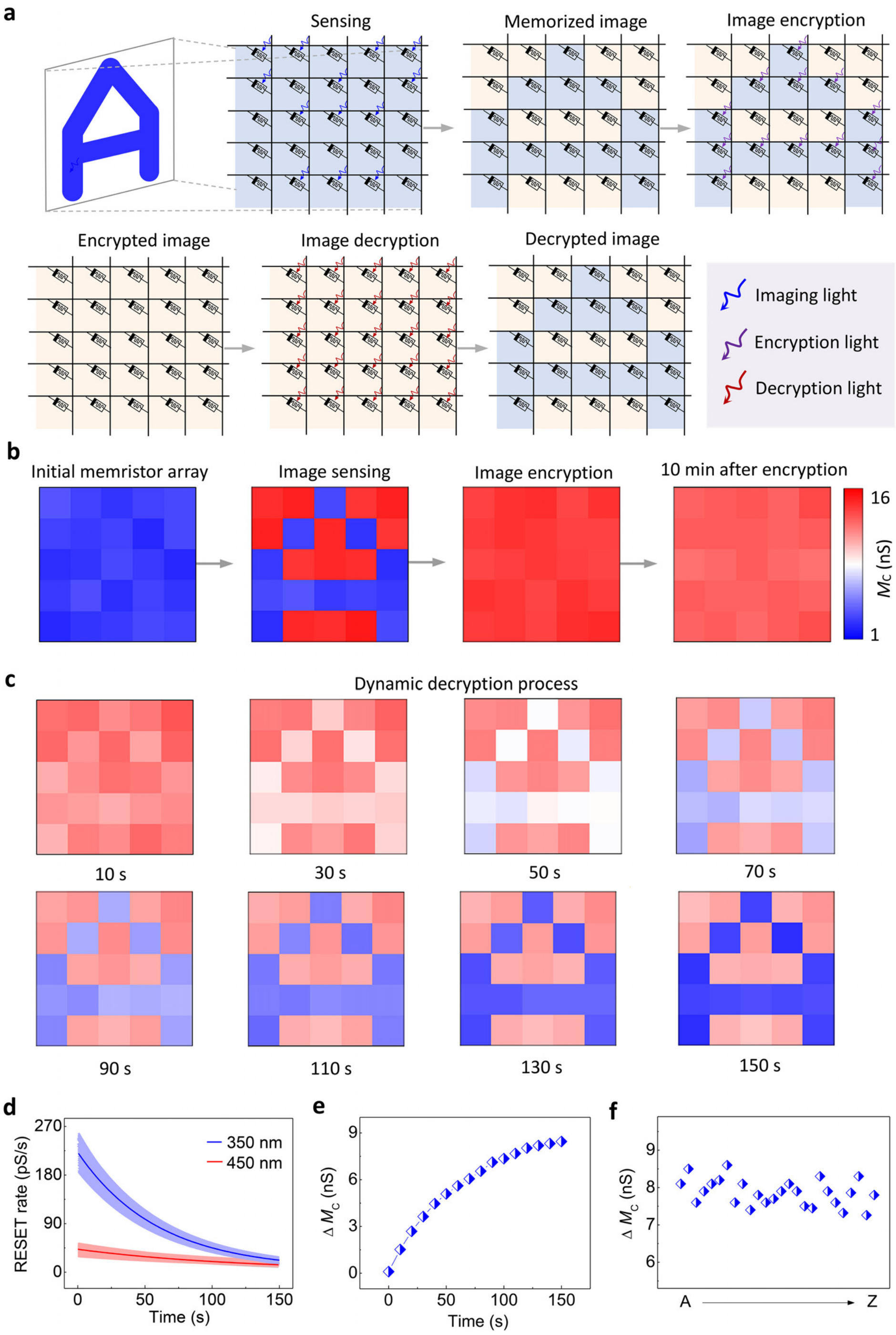

FIG. 3. *In situ* image encryption and decryption. (a) Schematic illustration of the in-pixel sensing, storage, encryption and decryption of the letter A via a 5 × 5 AOC memristor array. (b) Encryption process. Blue ($\lambda = 450$ nm, D = 25 s, and P = 30 μW cm^{-2}) and UV ($\lambda = 350$ nm, D = 15 s, and P = 20 μW cm^{-2}) light were used for imaging and encryption, respectively. After encryption, the memconductance of each pixel exhibits a consistent tendency, thus demonstrating good encrypted image retention performance (see the final image). (c) Dynamic decryption process with different light irradiation durations. Red light ($\lambda = 650$ nm and P = 30 μW cm^{-2}) was used for decryption. (d) Dependence of the RESET rate on decryption light irradiation duration. Data were from 25 devices in the array. The rate was calculated by the formula $|c\exp(-t/\tau)|$, where c and τ are constants and t is the time, which results from taking the derivative of the function $M_C = M_{C0} + M_{CA}\exp(-t/\tau)$ (Fig. S2). (e) Dependence of $\triangle M_C$ on decryption light irradiation duration. $\triangle M_C$ represents the difference between the average memconductance values of the imaging and encryption light-irradiated pixels. (f) $\triangle M_C$ values of all 26 letters from A to Z at a decryption light irradiation duration of 150 s.

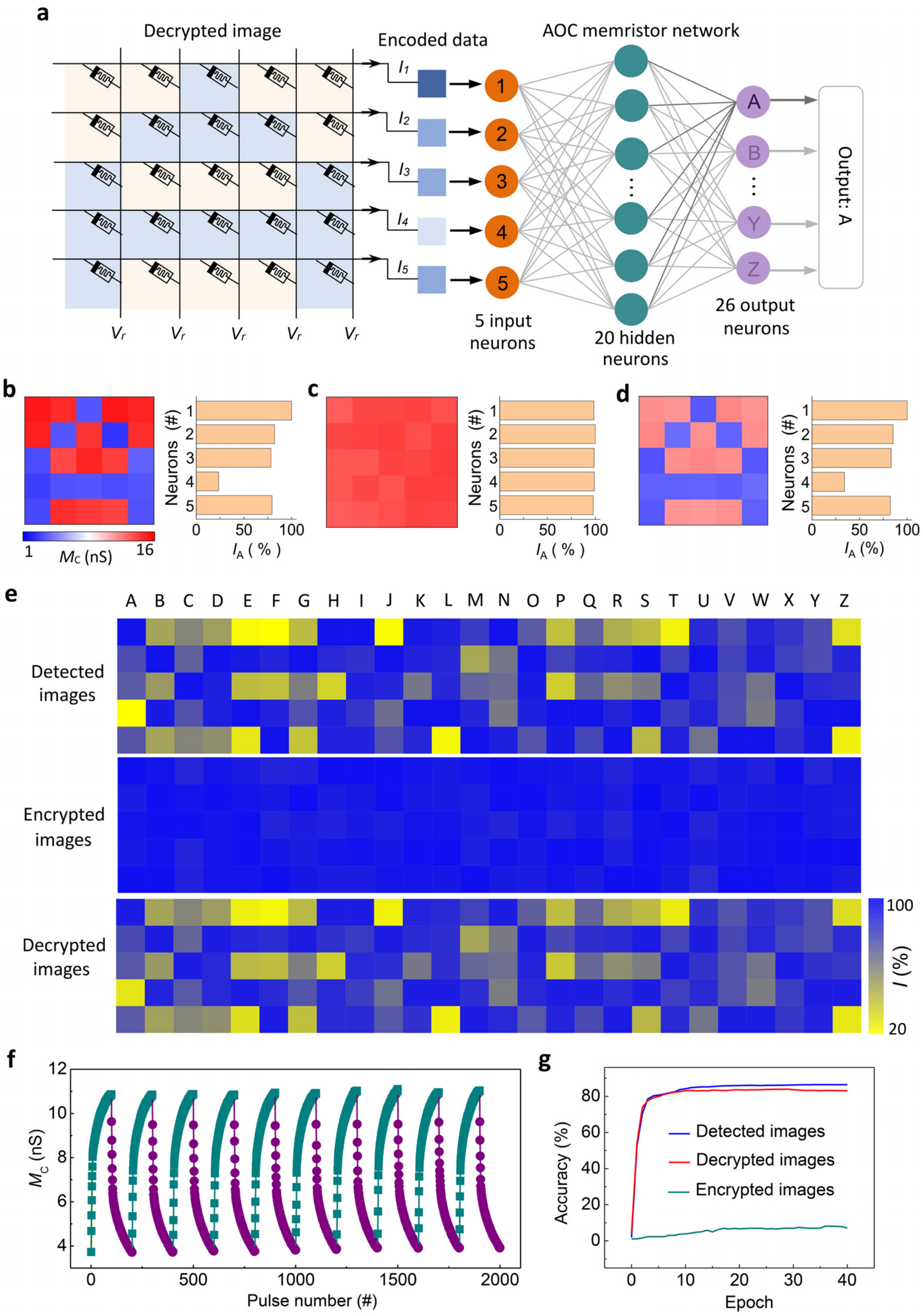

FIG. 4. Image encoding and recognition. (a) Schematic illustration of the encoding and recognition of a decrypted image of the letter A. For image encoding, the current value of each pixel was measured at 0.1 V. A five-dimensional feature vector was achieved through row-wise summation of the pixel currents. Image recognition was performed with an AOC memristor-based NCN. Encoding results of the detected (b), encrypted (c), and decrypted (d) images. Each feature vector was composed of five normalized current values. (e) Heatmaps of feature vectors of the detected (top panel), encrypted (middle panel), and decrypted (bottom panel) images of all 26 letters from A to Z. (f) Ten successive memconductance increase–decrease cycles of the AOC memristor. Reversible tuning of the memconductance was performed by means of 100 blue light pulses [$\lambda = 400$ nm, D = 1 s, pulse interval (PI) = 1 s, and P = 20 μW cm^{-2}] and 100 red light pulses ($\lambda = 650$ nm, D = 1 s, PI = 1 s, and P = 30 μW cm^{-2}). (g) Recognition results of the detected, encrypted, and decrypted images of all 26 letters in the alphabet.

large images of handwritten digits approach *ca.* 90% after three epochs, indicating the viability of the NCN for image recognition.

Then, the feature vectors of the 26 letters were fed into the NCN for training and recognition. As shown in Fig. 4(g), both the detected and decrypted images exhibit a similar recognition accuracy above 80% after six training epochs, demonstrating the efficacy of our in-sensor decryption scheme in restoring the original images. Furthermore, we assessed the image encryption strength by assuming that a hacker had access to the trained NCN. Even with 40 epochs, the recognition accuracy of the encrypted images remains below 10%, underscoring the high robustness of our in-sensor encryption scheme [Fig. 4(g)]. It is worth noting that the decryption light irradiation time significantly influences image decryption. Figure S10 presents the image recognition results at different irradiation times, showing that the accuracy increases from 10% at 10 s to 82% at 150 s. This irradiation time-sensitive recognition accuracy is conducive to further enhancing the security of the cryptography system.

In situ image destruction

Apart from encryption and decryption, reliable destruction of information is also important for information security.[52] From Figs. 2(f) and S3, we deduce that in our vision sensor, the encrypted and decrypted images can be destroyed *in situ* using only UV light irradiation. The encrypted and decrypted image destruction scheme is schematically illustrated in Fig. S11. The experimental results are shown in Figs. 5(a) and 5(b). Upon exposing all the pixels to the destruction light, both the encrypted and decrypted images of the letter A completely lose their characteristics. Even after decryption light irradiation, the images are not recoverable. To evaluate the strength of this in-sensor image destruction scheme, the trained NCN was used to recognize the destroyed images (see Materials and Methods). As shown in Figs. 5(c) and 5(d), the recognition accuracies for both encrypted and decrypted images are lower than 10%. This result highlights the effectiveness of our destruction scheme in ensuring the secure disposal of sensitive data.

Integrated image denoising and cryptography

For vision sensors, noise interference is usually inevitable. Our AOC memristor-based vison sensor offers an integrated solution for *in situ* image denoising and cryptography. Figure 6(a) schematically illustrates the physical realization of integrated image denoising and cryptography for the letter A. To denoise a noisy image, blue light is used to irradiate the noise pixels. Image denoising and encryption can be simultaneously performed with blue and UV light, respectively. Figure 6(b) shows the experimental results of noisy images with different noise levels represented by the number of noise pixels (see Materials and Methods). We observe that the denoising operation has no effect on the encryption efficacy. After decryption, the background noise is removed, and the image features become clearer. Figure 6(c) illustrates the NCN recognition accuracies of the noisy and denoised images (see Materials and Methods). Clearly, the denoised images have much higher recognition accuracies.

CONCLUSIONS

In summary, the neuromorphic vision sensor developed in this study, based on AOC memristors with unique PPPC and NPPC effects, enables several in-sensor operations such as storage, encryption, decryption, denoising, and destruction of visual images by only light irradiation. Using an AOC memristor-based NCN, this *in situ* image cryptography scheme proves to be highly robust against hacking attacks. The all-optical cryptographic operations possess the advantages of high speed, low energy consumption, and low hardware complexity, making this approach very promising for practical applications. Overall, the successful implementation of *in situ* image cryptography represents a significant milestone in the quest for comprehensive protection of visual information.

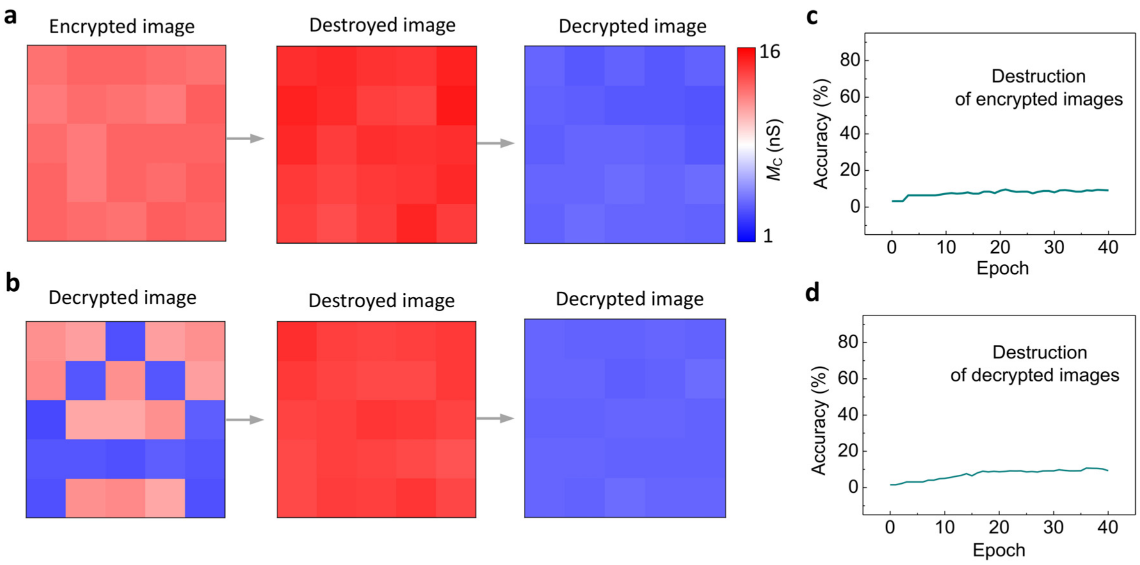

FIG. 5. *In situ* image destruction. Destruction of the encrypted (a) and decrypted (b) images of the letter A with UV light ($\lambda = 350$ nm, D = 15 s, and P = 20 μW cm^{-2}). Recognition results of the encrypted (c) and decrypted (d) images after destruction.

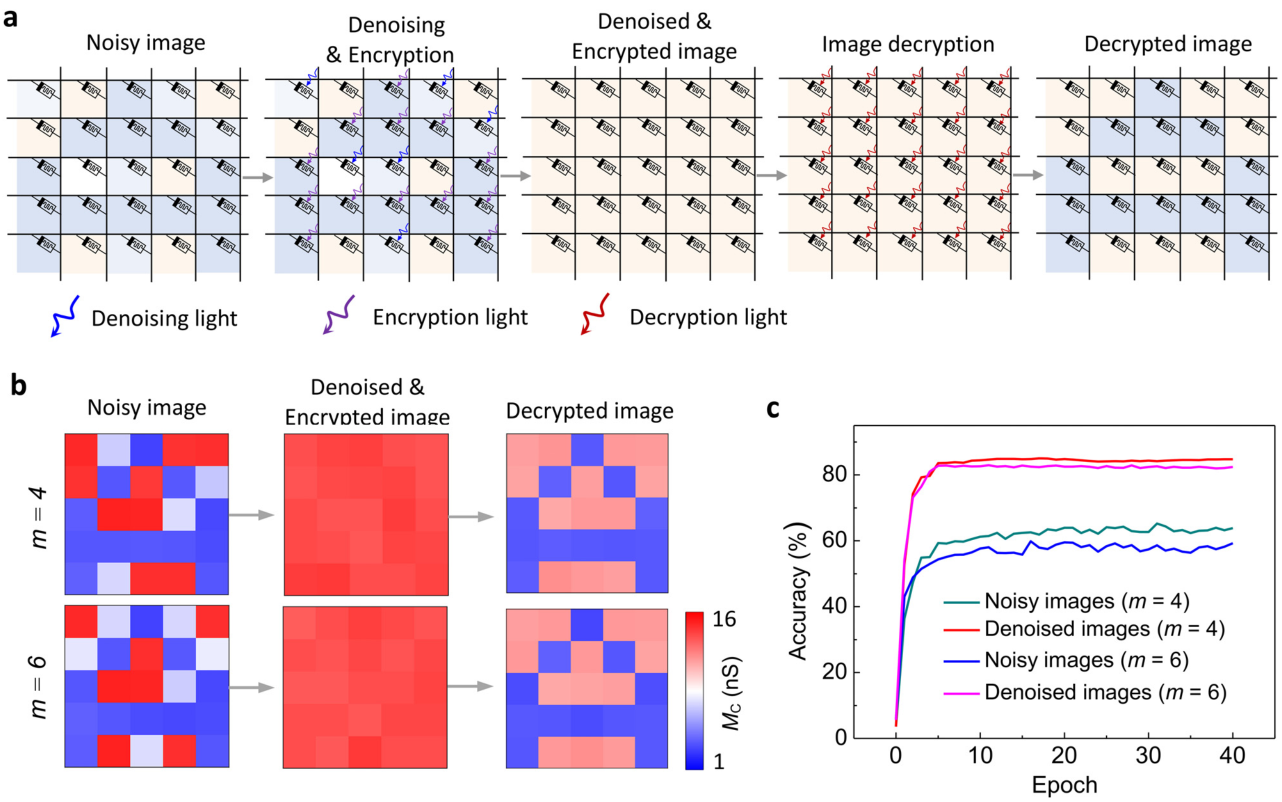

FIG. 6. Integrated *in situ* image denoising and cryptography. (a) Schematic illustration of the denoising, encryption and decryption of a noisy image of the letter A. (b) Experimental results of noisy images with two noise levels represented by the number of noise pixels (m). Blue light ($\lambda = 450$ nm, D = 25 s, and P = 30 μW cm^{-2}) was used to irradiate the noise pixels. (c) Recognition results of the noisy and denoised images.

MATERIALS AND METHODS

Device fabrication and characterization

IGZO thin films were deposited on Pt/Ti/SiO$_2$/Si substrates at room temperature (RT) via RF magnetron sputtering using a 99.99% pure InGaZnO$_4$ (In$_2$O$_3$:Ga$_2$O$_3$:ZnO = 1:1:2, molar ratio) target. The deposition was carried out under two different conditions: pure argon gas for O$_D$-IGZO and a mixture of argon and oxygen (in a 1:1 partial pressure ratio) for O$_R$-IGZO. The sputtering powers of the O$_D$-IGZO and O$_R$-IGZO films were 60 and 65 W, respectively, with a sputtering pressure of 0.5 Pa. The thicknesses of the O$_D$-IGZO and O$_R$-IGZO films were determined to be around 20 and 35 nm, respectively, using variable angle spectroscopic ellipsometry. As determined by Hall effect measurements, O$_D$-IGZO showed a low resistivity of about 10^{-2} Ω cm, and O$_R$-IGZO had a high resistivity (>10^5 Ω cm).

The AOC memristive devices were realized by depositing 10 nm thick Au top electrodes with a diameter of 100 μm onto the O$_D$-IGZO/O$_R$-IGZO films at RT via electron-beam evaporation with *in situ* metal shadow masks. The Au/O$_D$-IGZO/Pt and Au/O$_R$-IGZO/Pt devices were also fabricated. The sheet resistance and light transmittance of the Au film deposited on a quartz wafer were characterized by four-point probe sheet resistance measurement system (CRESBOX) and variable angle spectroscopic ellipsometry (M-2000 DI, J. A. Woollam Co., Inc.), respectively. The sheet resistance was about 10 Ω/□ and the average transmittance for light wavelengths ranging from 300 to 800 nm was > 55% (Fig. S12).

Electrical and optoelectronic measurements were conducted at RT in air using a Keithley 4200 semiconductor parameter analyzer equipped with a monochromatic light source. The top electrode was biased with a voltage while the bottom electrode (Pt) was grounded. The light entered the memristive device through the top electrode. For the Au/O$_D$-IGZO/Pt device, no photocurrent could be observed upon 350–650 nm light irradiation. As for the Au/O$_R$-IGZO/Pt device, a volatile photocurrent was generated upon 350–650 nm light illumination. The readout circuit of the 5 × 5 AOC memristor array is schematically illustrated in Fig. S6. The current readout process was performed cell-by-cell, similar to the operating mode of conventional optoelectronic detectors. The Au/O$_D$-IGZO/O$_R$-IGZO/Pt AOC memristors with a size of about 7.5 μm were also fabricated with *in situ* metal shadow masks (Fig. S13).

Image recognition

The three-layer NCNs in Figs. 4(a) and S9(a) were constructed using the CrossSim simulator.[53] The sigmoid activation function was used in the hidden and output layers. The learning rate was fixed at 0.1 for all experiments. For image recognition in Figs. 4(g) and S10, each database contained 18 200 images. For each letter in the alphabet, 699 images were generated using Python based on the results in Fig. 4(e), in which each image was generated by introducing stochastic noise to the detected, encrypted, or decrypted image feature vector. For each detected or decrypted letter, 500 images were used for training, and 200 images were used for recognition. For each encrypted letter, 500 detected and 200 encrypted images were used for training and recognition, respectively. In Figs. 5(c) and 5(d), 500 detected and 200 destroyed images of the letter A were used for training and recognition, respectively. In Fig. 6(b), noise pixels were randomly selected with memconductance in a range of 5–10 nS using Python. The corresponding memconductance values were written to the pixels using imaging light with different illumination times. In Fig. 6(c), 500 and 200 images of the letter A were used for training and recognition, respectively, for recognition of noisy and denoised letter A.

SUPPLEMENTARY MATERIAL

See the supplementary material for additional experimental data. Figure S1: Current–voltage characteristics of the AOC memristor in the dark. Figure S2: NPPC behavior of the AOC memristor after irradiation with SET light of different wavelengths. Figure S3: Two kinds of two-step optical SET and subsequent optical RESET processes of the AOC memristor. Figure S4: Current–voltage curves in the dark and under 650 nm light irradiation of Au/O_D-IGZO/O_R-IGZO/Pt AOC memristor. Figure S5: AOC memristor based on an O_D-IGZO/O_R-IGZO/O_D-IGZO trilayer structure. Figure S6: Readout circuit (left panel) and optical image (right panel; scale bar, 300 μm) of the 5 × 5 AOC memristor array. Figure S7: Memorization of the letter A. Figure S8: Imaging, encryption, and decryption of the letters from B to Z. Figure S9: Image recognition simulations. Figure S10: Dependence of the decrypted image recognition accuracy on the decryption light irradiation time. Figure S11: Schematic illustration of destruction schemes of the encrypted and decrypted images of the letter A. Figure S12: Optical transmittance spectrum of Au (10 nm)/quartz. Figure S13: Electrical and optoelectronic behavior of Au/O_D-IGZO/O_R-IGZO/Pt memristors with a size of about 7.5 μm.

ACKNOWLEDGMENTS

This work was partially supported by the National Natural Science Foundation of China (No. U20A20209), the Strategic Priority Research Program of Chinese Academy of Sciences (No. XDB32050204), the China National Postdoctoral Program for Innovative Talents (No. BX2021326), the China Postdoctoral Science Foundation (No. 2021M703310), the Zhejiang Provincial Natural Science Foundation of China (No. LQ22F040003), the Ningbo Natural Science Foundation of China (Nos. 2021J139 and 2023J356), and the State Key Laboratory for Environment-Friendly Energy Materials (No. 20kfhg09).

AUTHOR DECLARATIONS

Conflict of Interest

The authors have no conflicts to disclose.

Author Contributions

Lingxiang Hu: Conceptualization (lead); Data curation (lead); Formal analysis (lead); Funding acquisition (supporting); Investigation (lead); Methodology (lead); Project administration (lead); Software (equal); Validation (lead); Visualization (lead); Writing – original draft (lead); Writing – review & editing (lead). **Jiale Shao:** Data curation (supporting); Investigation (supporting); Methodology (supporting); Software (equal); Validation (supporting); Visualization (supporting); Writing – original draft (supporting). **Jingrui Wang:** Funding acquisition (supporting); Resources (equal); Writing – original draft (supporting); Writing – review & editing (supporting). **Peihong Cheng:** Resources (equal); Writing – original draft (supporting); Writing – review & editing (supporting). **Li Zhang:** Supervision (supporting); Writing – review & editing (equal). **Yang Chai:** Supervision (supporting); Writing – review & editing (equal). **Zhizhen Ye:** Supervision (equal); Writing – review & editing (supporting). **Fei Zhuge:** Conceptualization (lead); Formal analysis (equal); Funding acquisition (lead); Project administration (lead); Resources (lead); Supervision (lead); Validation (equal); Writing – original draft (equal); Writing – review & editing (equal).

DATA AVAILABILITY

The data that support the findings of this study are available from the corresponding author upon reasonable request.

REFERENCES

[1] M. M. Hossain, M. Fotouhi, and R. Hasan, "Towards an analysis of security issues, challenges, and open problems in the internet of things," in *IEEE World Congress on Services* (IEEE, 2015).

[2] J. Katz and Y. Lindell, *Introduction to Modern Cryptography* (CRC Press, 2014).

[3] L. Kocarev, "Chaos-based cryptography: A brief overview," IEEE Circuits Syst. Mag. **1**, 6–21 (2001).

[4] B. J. Mohd, T. Hayajneh, and A. V. Vasilakos, "A survey on lightweight block ciphers for low-resource devices: Comparative study and open issues," J. Network Comput. Appl. **58**, 73–93 (2015).

[5] V. A. Thakor, M. A. Razzaque, and M. R. A. Khandaker, "Lightweight cryptography algorithms for resource-constrained IoT devices: A review, comparison and research opportunities," IEEE Access **9**, 28177–28193 (2021).

[6] A. Dodda, N. Trainor, J. M. Redwing, and S. Das, "All-in-one, bio-inspired, and low-power crypto engines for near-sensor security based on two-dimensional memtransistors," Nat. Commun. **13**, 3587 (2022).

[7] B. Shao, T. Wan, F. Liao, B. J. Kim, J. Chen, J. Guo, S. Ma, J.-H. Ahn, and Y. Chai, "Highly trustworthy in-sensor cryptography for image encryption and authentication," ACS Nano **17**, 10291–10299 (2023).

[8] S. Wang, X. Pan, L. Lyu, C.-Y. Wang, P. Wang, C. Pan, Y. Yang, C. Wang, J. Shi, B. Cheng, W. Yu, S.-J. Liang, and F. Miao, "Nonvolatile van der Waals heterostructure phototransistor for encrypted optoelectronic logic circuit," ACS Nano **16**, 4528–4535 (2022).

[9] K.-H. Jeong, J. Kim, and L. P. Lee, "Biologically inspired artificial compound eyes," Science **312**, 557–561 (2006).

[10] H. C. Ko, M. P. Stoykovich, J. Song, V. Malyarchuk, W. M. Choi, C.-J. Yu, J. B. Geddes III, J. Xiao, S. Wang, Y. Huang, and J. A. Rogers, "A hemispherical electronic eye camera based on compressible silicon optoelectronics," Nature **454**, 748–753 (2008).

[11] Y. M. Song, Y. Xie, V. Malyarchuk, J. Xiao, I. Jung, K.-J. Choi, Z. Liu, H. Park, C. Lu, R.-H. Kim, R. Li, K. B. Crozier, Y. Huang, and J. A. Rogers, "Digital cameras with designs inspired by the arthropod eye," Nature **497**, 95–99 (2013).

[12] C. Posch, T. Serrano-Gotarredona, B. Linares-Barranco, and T. Delbruck, "Retinomorphic event-based vision sensors: Bioinspired cameras with spiking output," Proc. IEEE **102**, 1470–1484 (2014).

[13] S. Dong, T. Huang, and Y. Tian, "Spike camera and its coding methods," in *Data Compression Conference (DCC)* (IEEE, 2017).

[14] F. Zhou, Z. Zhou, J. Chen, T. H. Choy, J. Wang, N. Zhang, Z. Lin, S. Yu, J. Kang, H.-S. P. Wong, and Y. Chai, "Optoelectronic resistive random access memory for neuromorphic vision sensors," Nat. Nanotechnol. **14**, 776–782 (2019).

[15] L. Mennel, J. Symonowicz, S. Wachter, D. K. Polyushkin, A. J. Molina-Mendoza, and T. Mueller, "Ultrafast machine vision with 2D material neural network image sensors," Nature **579**, 62–66 (2020).

[16] M.-M. Poo, J.-L. Du, N. Y. Ip, Z.-Q. Xiong, B. Xu, and T. Tan, "China brain project: Basic neuroscience, brain diseases, and brain-inspired computing," Neuron **3**, 591–596 (2016).

[17] G. D. Field and E. J. Chichilnisky, "Information processing in the primate retina: Circuitry and coding," Annu. Rev. Neurosci. **30**, 1–30 (2007).

[18] F. Zhou and Y. Chai, "Near-sensor and in-sensor computing," Nat. Electron. **3**, 664–671 (2020).

[19] T. Wan, B. Shao, S. Ma, Y. Zhou, Q. Li, and Y. Chai, "In-sensor computing: Materials, devices, and integration technologies," Adv. Mater. **35**, 2203830 (2022).

[20] P. Maier, F. Hartmann, M. Emmerling, C. Schneider, M. Kamp, S. Höfling, and L. Worschech, "Electro-photo-sensitive memristor for neuromorphic and arithmetic computing," Phys. Rev. Appl. **5**, 054011 (2016).

[21] L. Hu, J. Yang, J. Wang, P. Cheng, L. O. Chua, and F. Zhuge, "All-optically controlled memristor for optoelectronic neuromorphic computing," Adv. Funct. Mater. **31**, 2005582 (2021).

[22] B. Cai, Y. Huang, L. Tang, T. Wang, C. Wang, Q. Sun, D. W. Zhang, and L. Chen, "All-optically controlled retinomorphic memristor for image processing and stabilization," Adv. Funct. Mater. **33**, 2306272 (2023).

[23] L. Sun, Z. Wang, J. Jiang, Y. Kim, B. Joo, S. Zheng, S. Lee, W. J. Yu, B.-S. Kong, and H. Yang, "In-sensor reservoir computing for language learning via two-dimensional memristors," Sci. Adv. **7**, eabg1455 (2021).

[24] J. Lao, M. Yan, B. Tian, C. Jiang, C. Luo, Z. Xie, Q. Zhu, Z. Bao, N. Zhong, X. Tang, L. Sun, G. Wu, J. Wang, H. Peng, J. Chu, and C. Duan, "Ultralow-power machine vision with self-powered sensor reservoir," Adv. Sci. **9**, 2106092 (2022).

[25] X. Shan, C. Zhao, X. Wang, Z. Wang, S. Fu, Y. Lin, T. Zeng, X. Zhao, H. Xu, X. Zhang, and Y. Liu, "Plasmonic optoelectronic memristor enabling fully light-modulated synaptic plasticity for neuromorphic vision," Adv. Sci. **9**, 2104632 (2022).

[26] H. Tan, Y. Zhou, Q. Tao, J. Rosen, and S. Dijken, "Bioinspired multisensory neural network with crossmodal integration and recognition," Nat. Commun. **12**, 1120 (2021).

[27] Y. Wang, Y. Gong, S. Huang, X. Xing, Z. Lv, J. Wang, J.-Q. Yang, G. Zhang, Y. Zhou, and S.-T. Han, "Memristor-based biomimetic compound eye for real-time collision detection," Nat. Commun. **12**, 5979 (2021).

[28] J. Yang, L. Hu, L. Shen, J. Wang, P. Cheng, H. Lu, F. Zhuge, and Z. Ye, "Optically driven intelligent computing with ZnO memristor," Fundam. Res. (in press 2022).

[29] Y. Sun, Q. Li, X. Zhu, C. Liao, Y. Wang, Z. Li, S. Liu, H. Xu, and W. Wang, "In-sensor reservoir computing based on optoelectronic synapse," Adv. Intell. Syst. **5**, 2200196 (2023).

[30] H. Jang, H. Hinton, W.-B. Jung, M.-H. Lee, C. Kim, M. Park, S.-K. Lee, S. Park, and D. Ham, "In-sensor optoelectronic computing using electrostatically doped silicon," Nat. Electron. **5**, 519–525 (2022).

[31] Z. Zhang, S. Wang, C. Liu, R. Xie, W. Hu, and P. Zhou, "All-in-one two-dimensional retinomorphic hardware device for motion detection and recognition," Nat. Nanotechnol. **17**, 27–32 (2022).

[32] C.-Y. Wang, S.-J. Liang, S. Wang, P. Wang, Z. Li, Z. Wang, A. Gao, C. Pan, C. Liu, J. Liu, H. Yang, X. Liu, W. Song, C. Wang, B. Cheng, X. Wang, K. Chen, Z. Wang, K. Watanabe, T. Taniguchi, J. J. Yang, and F. Miao, "Gate-tunable van der Waals heterostructure for reconfigurable neural network vision sensor," Sci. Adv. **6**, eaba6173 (2020).

[33] L. Pi, P. Wang, S.-J. Liang, P. Luo, H. Wang, D. Li, Z. Li, P. Chen, X. Zhou, F. Miao, and T. Zhai, "Broadband convolutional processing using band-alignment-tunable heterostructures," Nat. Electron. **5**, 248–254 (2022).

[34] K. Liu, T. Zhang, B. Dang, L. Bao, L. Xu, C. Cheng, Z. Yang, R. Huang, and Y. Yang, "An optoelectronic synapse based on α-In_2Se_3 with controllable temporal dynamics for multimode and multiscale reservoir computing," Nat. Electron. **5**, 761–773 (2022).

[35] H. Jang, C. Liu, H. Hinton, M.-H. Lee, H. Kim, M. Seol, H.-J. Shin, S. Park, and D. Ham, "An atomically thin optoelectronic machine vision processor," Adv. Mater. **32**, 2002431 (2020).

[36] J. Meng, T. Wang, H. Zhu, L. Ji, W. Bao, P. Zhou, L. Chen, Q.-Q. Sun, and D. W. Zhang, "Integrated in-sensor computing optoelectronic device for environment-adaptable artificial retina perception application," Nano Lett. **22**, 81–89 (2022).

[37] T. Ahmed, M. Tahir, M. X. Low, Y. Ren, S. A. Tawfik, E. L. H. Mayes, S. Kuriakose, S. Nawaz, M. J. S. Spencer, H. Chen, M. Bhaskaran, S. Sriram, and S. Walia, "Fully light-controlled memory and neuromorphic computation in layered black phosphorus," Adv. Mater. **33**, 2004207 (2021).

[38] C. Choi, J. Leem, M. S. Kim, A. Taqieddin, C. Cho, K. W. Cho, G. J. Lee, H. Seung, H. J. Bae, Y. M. Song, T. Hyeon, N. R. Aluru, S. W. Nam, and D.-H. Kim, "Curved neuromorphic image sensor array using a MoS_2-organic heterostructure inspired by the human visual recognition system," Nat. Commun. **11**, 5934 (2020).

[39] Y.-X. Hou, Y. Li, Z.-C. Zhang, J.-Q. Li, D.-H. Qi, X.-D. Chen, J.-J. Wang, B.-W. Yao, M.-X. Yu, T.-B. Lu, and J. Zhang, "Large-scale and flexible optical synapses for neuromorphic computing and integrated visible information sensing memory processing," ACS Nano **15**, 1497–1508 (2021).

[40] F. Liao, Z. Zhou, B. J. Kim, J. Chen, J. Wang, T. Wan, Y. Zhou, A. T. Hoang, C. Wang, J. Kang, J.-H. Ahn, and Y. Chai, "Bioinspired in-sensor visual adaptation for accurate perception," Nat. Electron. **5**, 84–91 (2022).

[41] H. Li, X. Jiang, W. Ye, H. Zhang, L. Zhou, F. Zhang, D. She, Y. Zhou, and S.-T. Han, "Fully photon modulated heterostructure for neuromorphic computing," Nano Energy **65**, 104000 (2019).

[42] S. Seo, S.-H. Jo, S. Kim, J. Shim, S. Oh, J.-H. Kim, K. Heo, J.-W. Choi, C. Choi, S. Oh, D. Kuzum, H.-S. P. Wong, and J.-H. Park, "Artificial optic-neural synapse for colored and color-mixed pattern recognition," Nat. Commun. **9**, 5106 (2018).

[43] B. Dang, K. Liu, X. Wu, Z. Yang, L. Xu, Y. Yang, and R. Huang, "One-phototransistor–one-memristor array with high-linearity light-tunable weight for optic neuromorphic computing," Adv. Mater. **35**, 2204844 (2022).

[44] D. Lee, M. Park, Y. Baek, B. Bae, J. Heo, and K. Lee, "In-sensor image memorization and encoding via optical neurons for bio-stimulus domain reduction toward visual cognitive processing," Nat. Commun. **13**, 5223 (2022).

[45] Z. Zhang, X. Zhao, X. Zhang, X. Hou, X. Ma, S. Tang, Y. Zhang, G. Xu, Q. Liu, and S. Long, "In-sensor reservoir computing system for latent fingerprint recognition with deep ultraviolet photo-synapses and memristor array," Nat. Commun. **13**, 6590 (2022).

[46] B. Ryu, H.-K. Nohet, E.-A. Choi, and K. J. Chang, "O-vacancy as the origin of negative bias illumination stress instability in amorphous In–Ga–Zn–O thin film transistors," Appl. Phys. Lett. **97**, 022108 (2010).

[47] H.-K. Noh, K. J. Chang, B. Ryu, and W.-J. Lee, "Electronic structure of oxygen-vacancy defects in amorphous In–Ga–Zn–O semiconductors," Phys. Rev. B **84**, 115205 (2011).

[48] S. Jeon, S.-E. Ahn, I. Song, C. J. Kim, U.-I. Chung, E. Lee, I. Yoo, A. Nathan, S. Lee, J. Robertson, and K. Kim, "Gated three-terminal device architecture to eliminate persistent photoconductivity in oxide semiconductor photosensor arrays," Nat. Mater. **11**, 301–305 (2012).

[49] H. Oh, S.-M. Yoon, M. K. Ryu, C.-S. Hwang, S. Yang, and S.-H. K. Park, "Photon-accelerated negative bias instability involving subgap states creation in amorphous In–Ga–Zn–O thin film transistor," Appl. Phys. Lett. **97**, 183502 (2010).

[50] K. Bache and M. Lichman, *UCI Machine Learning Repository* (University of California at Irvine, School of Information and Computer Science, Irvine, CA, 2016).

[51] Y. Lecun, C. Cortes, and C. J. Burges, *The MNIST Database of Handwritten Digits* (National Institute of Standards and Technology, Gaithersburg, MD, 2016).

[52] H. Jiang, C. Li, R. Zhang, P. Yan, P. Lin, Y. Li, J. J. Yang, D. Holcomb, and Q. Xia, "A provable key destruction scheme based on memristive crossbar arrays," Nat. Electron. **1**, 548–554 (2018).

[53] See https://cross-sim.sandia.gov for "CrossSim Simulator" (2021).